JOURNAL OF GEOPHYSICAL RESEARCH, VOL. 100, NO. B1, PAGES 365–378, JANUARY 10, 1995

Comprehensive analysis of marine magnetic vector anomalies

J. Korenaga[1]

Ocean Research Institute, University of Tokyo, Tokyo, Japan

Abstract. We present a comprehensive description of the analysis of marine magnetic vector anomalies. The marine magnetic vector field can be measured with a shipboard three-component magnetometer (STCM). The STCM has the advantage of measuring three components, but it suffers from several types of noise sources because the principles of its measurement are more complex than that of a proton-precession magnetometer. We have estimated the quality of STCM data, constructed an optimal filter, and evaluated the reliability of the filtered data. Then, we have organized an analytical procedure composed of four steps: (1) the discrimination between two- and three- dimensional magnetic sources; (2) the determination of magnetic boundaries; (3) the calculation of the boundary strikes; and (4) the estimation of the boundary magnetization contrasts. We show examples of these procedures using the data near the East Pacific Rise 28°S-31°S collected during leg 5 of the GLORIA expedition. All the results of the above processing are merged in order to illustrate the distinct pattern of the seafloor magnetization in the surveyed area.

Introduction

The magnetic anomaly field is a vector field. Because total intensity measurements of the magnetic field with a proton-precession magnetometer (PPM) are easily conducted and the PPM stably provides data of high resolution (a few nanoteslas), marine magnetic anomalies have been conventionally studied with total intensity data. However, several limitations arise in the analysis of total intensity anomalies. One commonly recognized problem is that the PPM only measures the components of the anomaly in the direction of Earth's main field. As an extreme example, anomalous fields cannot be detected with total intensity measurements at points where the anomalous field is normal to the total field. In the case of marine magnetic anomalies, total intensity measurements strongly depend on on the geometry of magnetic stripes. In addition, the two dimensionality of seafloor magnetization cannot be established unless there is good correspondence between adjacent profiles. Poor correspondence will result, for example, where the seafloor has undergone intense deformations due to plate boundary reorganization, such as those that occur near propagating rifts or microplates. Without dense track coverage, the tectonic interpretation of magnetic anomalies in such areas is speculative at best.

A shipboard three-component magnetometer (STCM) has been developed by *Isezaki* [1986] in order to overcome the above limitations and to provide a more effective approach to the study of marine magnetic anomalies. Although airborne three-component magnetometers have been used in the past to survey marine magnetic anomalies [e.g., *Blakely et al.*, 1973], shipborne surveys have the advantage of being able to collect ancillary data (e.g., bathymetry) simultaneously. Several authors have worked on STCM data and indicated some important features of the vector anomalies [e.g., *Seama and Isezaki*, 1990; *Seama et al.*, 1993], but systematic applications of STCM data to tectonic processes have not yet been developed.

In this paper, we provide a newly established analytical system for STCM data to extract a clear image of seafloor magnetization, even from sparse profiles. First, we describe how to evaluate the quality of STCM data using power spectral analysis. The measurement error of STCM can be estimated by coherency calculation between STCM data and ship attitude data and by comparing the total intensity anomaly calculated from STCM data with that from an independent PPM. An optimal filter can be directly constructed by the above error estimation. Using the total power of residual noise, we also define absolute amplitude error and relative variation error. Then we present an inversion technique to extract the information of magnetic boundaries in terms of their positions, strikes, and magnetization contrasts. This inversion is limited to two-dimensional treatments, but we also provide a method to test the two-dimensional assumption with a two- and three-dimensional (2-D/3-D) magnetic source discrimination scheme. Finally, we apply these methods to STCM data obtained from the southern East Pacific Rise during leg 5 of the GLORIA expedition.

Data Inspection

Principle of a Shipboard Three-Component Magnetometer

Two major difficulties arise in measuring a magnetic vector field at sea: the motion of the ship and its magnetization.

[1] Now at MIT/WHOI Joint Program, Massachusetts Institute of Technology, Cambridge, Massachusetts.

Copyright 1995 by the American Geophysical Union.

Paper number 94JB02596.
0148-0227/95/94JB-02596$05.00

The STCM system solves the first of these problems by measuring the magnetic vector field and ship's attitude simultaneously. The STCM system includes a triaxial fluxgate magnetometer, a horizontal gyroscope, and a vertical gyroscope. Simultaneous data logging is controlled by a computer unit as illustrated in the schematic diagram of Figure 1.

It is relatively more complicated to remove the influence of the ship's magnetization. The observed magnetic field onboard is the sum of the ambient geomagnetic field in the ship's coordinates and the induced and permanent magnetic field of the ship body. This is expressed as follows [*Isezaki*, 1986]:

$$\boldsymbol{H}_{\text{obs}} = RPY\boldsymbol{F} + ARPY\boldsymbol{F} + \boldsymbol{H}_p, \qquad (1)$$

where $\boldsymbol{F}$ is the ambient geomagnetic field vector, A is the induced magnetization matrix, $\boldsymbol{H}_p$ is the permanent magnetic field vector, and R, P, and Y are the matrices of rotation due to the roll, pitch and yaw, respectively, of the ship. If A and $\boldsymbol{H}_p$ are time-independent and the true geomagnetic field vectors at four locations are known, the unknown parameters in equation (1), A and $\boldsymbol{H}_p$, can be calculated from the observations at these four locations. In reality, however, those unknown parameters are time-dependent because of the viscous remanent magnetization (VRM) of the ship, and the true geomagnetic vector fields cannot be determined from shipboard measurements.

We assume that the VRM affects A and $\boldsymbol{H}_p$ gradually rather than rapidly, and that the International Geomagnetic Reference Field (IGRF) [*International Association of Geomagnetism and Aeronomy Division V*, 1991] represents the true geomagnetic field. A single set of A and $\boldsymbol{H}_p$ is estimated from a least squares inversion using the data obtained in a special navigation maneuver called a "figure eight", during which the ship first steams in a circle clockwise (or counterclockwise), and then makes a circle in the opposite direction at the standard cruising speed. These double circles are designed to acquire unbiased ship's rolling; when the ship turns clockwise, it tends to incline toward the starboard side, and vice versa. Figure eights are usually conducted as frequently as possible during a survey.

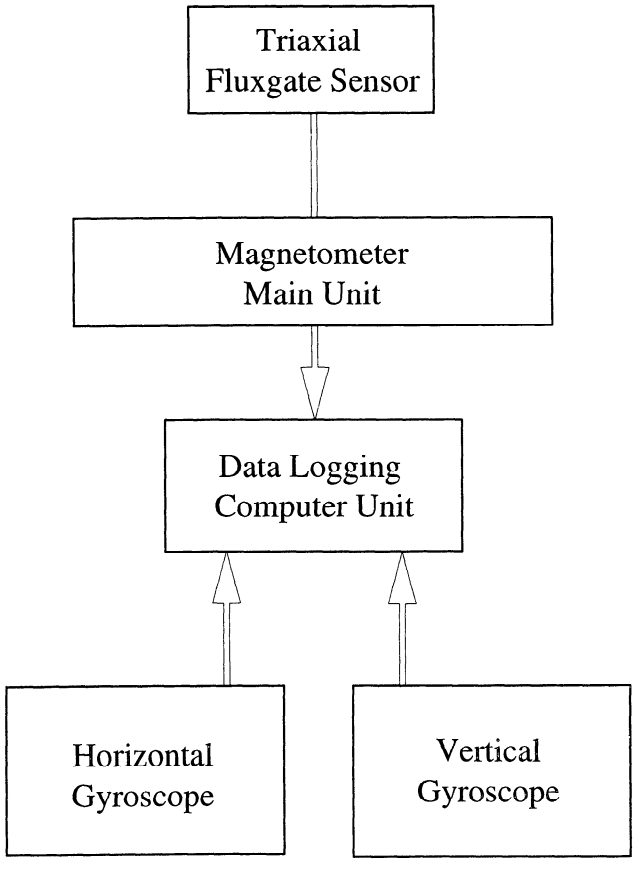

Figure 1. Schematic diagram of the STCM system.

Quality of Data

Noise sources. The difficulties described above produce a great variety of noise in STCM profiles. A measurement error of 0.1° in ship's attitude in an ambient field of 25,000 nT results in a 40-nT error in the STCM profile. In addition, it is difficult to simultaneously log attitude and fluxgate data. When the ship is rolling from -5° to +5° with a period of 10 s, a sampling gap of 50 ms is equivalent to a 0.05° error in the ship's attitude. Ship motion typically has a period from a few seconds to a few minutes, and the resulting noise occurs in a similar band.

Two other noise sources are present in equation (1). First, the IGRF used to find A and $\boldsymbol{H}_p$ does not account for local magnetic anomalies at the location of a figure eight rotation. Second, equation (1) does not account for VRM of the ship, and thus A and $\boldsymbol{H}_p$ may change gradually after a figure eight. Errors in A cause noise of various wavelengths corresponding to lateral variation of geomagnetic field, and those in $\boldsymbol{H}_p$ add bias and drift to the data.

Noise power spectra. Our task is to construct a filter to remove these numerous kinds of noise from the data. *Blakely et al.* [1973] used the power spectrum of the data to discriminate signal from noise, applying the fact that the slope of the natural logarithm of a power spectrum is related to the depth of magnetic sources [*Spector and Grant*, 1970]. Unfortunately, the power spectrum of STCM data is too complicated to use this technique. The measurement error of STCM can be expressed as

$$\Delta\boldsymbol{F} = \hat{\Theta}^{-1}\hat{A}'^{-1}(A'\Theta\boldsymbol{F} + \boldsymbol{H}_p - \hat{\boldsymbol{H}}_p) - \boldsymbol{F}, \qquad (2)$$

where Θ and A' denote RPY and $A + I$, respectively, and where $\hat{\Theta}$, $\hat{A}$ and $\hat{\boldsymbol{H}}_p$ are measured ship attitude matrix and estimated ship magnetization factors, respectively. Estimation errors of ship magnetization factors introduce noise which correlates with the ship motion. Measurement errors in ship attitude data also produce the noise of the same character assuming that the errors are correlated with the ship motion. The power of the noise correlated with the ship motion (N_Θ) can be estimated by calculating the coherency between STCM data and ship attitude data as follows:

$$\begin{aligned} |N_\Theta(k)|^2 &= |F_x(k)|^2\text{coh}(F_x,\Theta) + |F_y(k)|^2\text{coh}(F_y,\Theta) \\ &\quad + |F_z(k)|^2\text{coh}(F_z,\Theta), \end{aligned} \qquad (3)$$

where k is wavenumber; $F_x(k)$, $F_y(k)$, and $F_z(k)$ are the observed north, east, and downward anomalies, respectively, in the wavenumber domain; and $\text{coh}(F_x,\Theta)$, $\text{coh}(F_y,\Theta)$,

and $\mathrm{coh}(F_z, \Theta)$ are squared coherency between the observed magnetic anomalies and the ship attitude data. Each coherency is the highest value of the coherency with yaw, roll, and pitch.

The measurement error which cannot be detected by the above procedure (e.g., $\hat{A}'^{-1}A' = kI$ and $k \neq 1$) can be estimated by comparing the total intensity anomaly calculated from STCM data (F_{STCM}) with that from a PPM (F_{PPM}) as follows:

$$|N_S(k)|^2 = |D(k)|^2[1 - \mathrm{coh}(D, \Theta)], \tag{4}$$

where $N_S(k)$ and $D(k)$ are the noise associated with the scaling error and the difference between F_{STCM} and F_{PPM}, respectively. The term $[1 - \mathrm{coh}(D, \Theta)]$ is required because F_{STCM} is influenced by the ship motion as

$$F_{\mathrm{STCM}} = |\hat{A}'^{-1}(A'\Theta\boldsymbol{F} + \boldsymbol{H}_p - \hat{\boldsymbol{H}}_p)| - F_{\mathrm{IGRF}} \tag{5}$$

where F_{IGRF} is the total intensity of the IGRF.

It is noted that a power spectrum estimated from the fast Fourier transform (FFT) of a single profile is quite unreliable, each point having a standard deviation to its value, but standard deviation can be reduced by $1/\sqrt{N}$ by averaging the spectra of N profiles. Thus we should estimate and average the power spectra of as many sample profiles as possible from the survey, while keeping the length of each profile longer than the scale of typical anomaly variations in the surveyed area.

Construction of Optimal Filter

The influence of noise on signal is evaluated by the signal to noise ratio (S/N), not by the noise power itself. Optimal filtering, also known as Wiener filtering, utilizes the concept of S/N and is defined in the wavenumber domain as [*Press et al.*, 1992]

$$\Phi(k) = \frac{|S(k)|^2}{|S(k)|^2 + |N(k)|^2}, \tag{6}$$

where $\Phi(k)$, $S(k)$, and $N(k)$ are the optimal filter, the signal, and the noise, respectively, in the wavenumber domain. It is noted that this formula is based on the assumption that signal and noise are not correlated. Using the two kinds of noise power defined in the previous section, the optimal filter for STCM data can be constructed as

$$\begin{aligned}\Phi(k) &= \Phi_\Theta(k)\Phi_S(k) \\ &= \left(\frac{|F_x(k)|^2 + |F_y(k)|^2 + |F_z(k)|^2 - |N_\Theta(k)|^2}{|F_x(k)|^2 + |F_y(k)|^2 + |F_z(k)|^2}\right) \\ &\quad \cdot \left(\frac{|F_{\mathrm{PPM}}(k)|^2}{|F_{\mathrm{PPM}}(k)|^2 + |N_S(k)|^2}\right),\end{aligned} \tag{7}$$

where $\Phi_\Theta(k)$ and $\Phi_S(k)$ are optimal filters related to $N_\Theta(k)$ and $N_S(k)$, respectively.

Error Level of Filtered Data

The reliability of filtered data can be assessed using the residual noise power, which is expressed as $\Phi(k)|N(k)|^2$. The absolute amplitude error (ΔEa) of filtered data is defined as the square root of the total power of this residual noise,

$$\Delta Ea = \left[\int_{-k_{Nq}}^{k_{Nq}} \Phi(k)|N(k)|^2 dk\right]^{\frac{1}{2}}, \tag{8}$$

where k_{Nq} is the Nyquist wavenumber and $|N(k)|^2 = |N_\Theta(k)|^2 + |N_S(k)|^2$.

The residual low wavenumber noise can be reduced to some extent by spatial differentiation along a profile. The relative variation error (ΔEr) can be estimated by

$$\Delta Er = \left[\int_{-k_{Nq}}^{k_{Nq}} k^2\Phi(k)|N(k)|^2 dk\right]^{\frac{1}{2}}, \tag{9}$$

where the factor k^2 comes from the differentiation of $|N(k)|^2$. If the noise has strong power even in the lower wavenumber, the absolute amplitude error will increase when the length of a sample profile becomes longer. However, the relative variation error will not be affected by the length because of the factor k^2 in equation (9).

The error of each component of magnetic anomaly field ($\Delta E_x, \Delta E_y$, and ΔE_z) is obtained from ΔEa or ΔEr by multiplying $1/\sqrt{3}$, assuming that the measurement error is equally distributed over the three components.

Data Analysis

Discrimination of 2-D/3-D Magnetic Sources

A prominent feature of marine magnetic anomalies is their two dimensionality, and this has played a very important role in the advent and development of plate tectonics [e.g., *Vine and Matthews*, 1963]. The linear character of seafloor magnetization, responsible for the two-dimensional anomalies, depends on the mechanisms of seafloor spreading at mid-ocean ridges. Propagating rifts [*Hey et al.*, 1980] and overlapping spreading centers [*Macdonald and Fox*, 1983; *Lonsdale*, 1983] perturb this 2-D geometry, and other processes such as seamount formation produce three-dimensional magnetic sources.

Magnetic vector anomalies provide information to discriminate between 2-D and 3-D magnetic sources. The magnetic field of 2-D magnetic sources has a remarkable feature; the sources produce no magnetic field parallel to their long axis, and the vertical component can be transformed to the horizontal component by multiplying by $i\mathrm{sgn}(k)$ in the frequency domain [*Isezaki*, 1986]. Assuming 2-D magnetic sources, the horizontal component ($H_{2\mathrm{D}}$) can be calculated from the observed vertical component ($F_{z,\mathrm{obs}}$) in the wavenumber domain by,

$$H_{2\mathrm{D}}(k) = i\mathrm{sgn}(k)F_{z,\mathrm{obs}}(k), \tag{10}$$

while the observed horizontal component (H_{obs}) is calculated in the space domain by

$$|H_{\mathrm{obs}}(p)| = \sqrt{F_{x,\mathrm{obs}}^2(p) + F_{y,\mathrm{obs}}^2(p)}, \tag{11}$$

where p, $F_{x,\mathrm{obs}}$, and $F_{y,\mathrm{obs}}$ are the coordinate along the ship track and the observed north and east components, respectively. It is noted that the sign of H_{obs} cannot be determined

for arbitrary magnetic field; thus we also take the absolute value of H_{2D}. The deviation of $|H_{obs}|$ from $|H_{2D}|$ indicates the significance of three dimensional sources. Since $|H_{2D}|$ and $|H_{obs}|$ have errors of ΔE_z and $\sqrt{\Delta E_x^2 + \Delta E_y^2}$, respectively, the comparison between $|H_{2D}|$ and $|H_{obs}|$ has an error of $\Delta E_z + \sqrt{\Delta E_x^2 + \Delta E_y^2}$, which can be simplified to $(1 + \sqrt{2})\Delta Ea/\sqrt{3}$. Using this error level as a criterion of the two dimensionality, we define the 3-D index in the space domain as

$$I_{3D}(p) = \frac{\sqrt{3}}{(1+\sqrt{2})\Delta Ea} \left| |H_{obs}| - |H_{2D}| \right|. \quad (12)$$

Observed fields where I_{3D} is less than unity are regarded as two-dimensional.

Detection of Magnetic Boundaries

During seafloor spreading, geomagnetic field reversals are recorded as magnetization contrasts. Analysis of marine magnetic anomalies thus can determine magnetic isochrons, the key to solving the history of seafloor evolution. Observed total intensity anomalies have been conventionally used in this procedure, and a reference 2-D block model of seafloor magnetization is usually computed for comparison.

Another approach to identify magnetic isochrons using magnetic vector anomalies was proposed by *Seama et al.* [1993]. The intensity of spatial differential vectors (ISDV) has its maximum at a magnetic boundary, irrespective of the direction of the magnetization [see *Seama et al.*, 1993, Figure 2]. The ISDV is defined as follows:

$$\left|\frac{\partial \boldsymbol{F}}{\partial p}\right| = \sqrt{\left(\frac{\partial F_x}{\partial p}\right)^2 + \left(\frac{\partial F_y}{\partial p}\right)^2 + \left(\frac{\partial F_z}{\partial p}\right)^2} \quad (13)$$

where F_x, F_y, and F_z are the north, east, and downward components of observed geomagnetic anomaly field, respectively, and p is the coordinate along a ship track. Thus the magnetic boundaries in a surveyed area can be easily detected by calculating the ISDV along a profile. Since noise in data may also create some peaks in the ISDV profile, it is necessary to develop a threshold for significant peaks. The relative variation error (ΔEr) can be used for this purpose.

The ISDV is similar to analytic signal [*Nabighan*, 1972], although the former is used to interpret a potential vector field and the latter a potential scalar field, and both quantities lose their resolution for closely spaced magnetic boundaries. *Atchuta Rao et al.* [1981] showed that two maxima in analytic signal merge into one for a dike whose half width is equal to or less than its depth of burial. Here we calculated a position error in the ISDV peak detection using a simplified model illustrated in Figure 2. The model has two boundaries with equal magnetization contrast, which are located $2L$ apart. The mean depth to the magnetic layer is D, and the layer thickness is H. The position error (Δp) is

$$\Delta p = L - \left[\frac{L^2}{3} - D^2 + \frac{2L}{3}\sqrt{L^2 + 3D^2}\right]^{\frac{1}{2}} \quad (14)$$

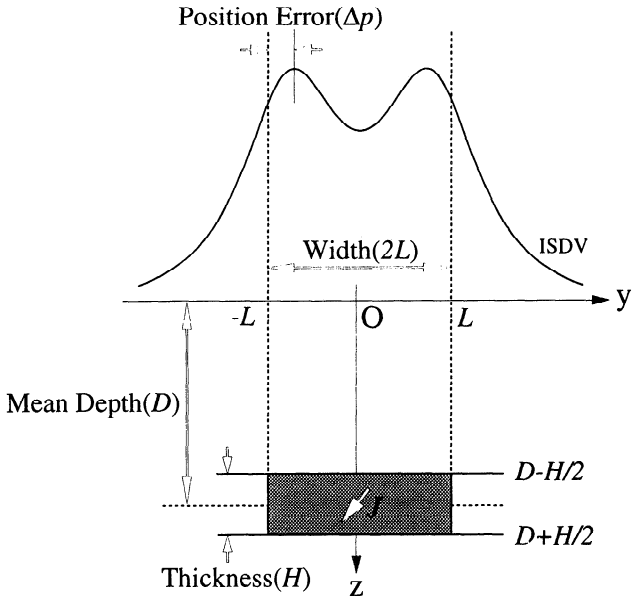

Figure 2. Simplified model with two magnetic boundaries separated by distance $2L$. Layer thickness is H, and mean depth to the layer is D. Magnetization of the layer is $\boldsymbol{J}$. Position error (Δp) is defined as difference between actual boundary and ISDV peak position.

(see Appendix A). The second term in the right-hand side of (14) is imaginary when

$$L < (2\sqrt{3} - 3)^{\frac{1}{2}} D \sim 0.68D, \quad (15)$$

i.e., the ISDV shows only one maximum for two boundaries with such an interval. The result of the model calculation is summarized in Figure 3. Approximately, the ISDV shows two maxima with a negligible error ($\leq$ 0.2 km) when two boundaries are located more than $5(D - 1)$ km apart.

The above error estimation assumes that reversal boundaries are abrupt and vertical. A finite transition width decreases the ISDV maximum, and an oblique boundary slightly displaces the peak position [*Seama et al.*, 1993]. The former effect widens the single domain region in Figure 3, and the latter increases the position error.

Calculation of the Strikes of Magnetic Boundaries

We now introduce the concept of a magnetic conjugate source, which models a single magnetization contrast as two juxtaposed slabs each with uniform magnetization and constant thickness (Figure 4). The magnetization vectors ($\boldsymbol{J}_l$ and $\boldsymbol{J}_r$) are parallel or antiparallel to each other, and the magnetic contrast vector ($\delta \boldsymbol{J}$) is defined as $\boldsymbol{J}_r - \boldsymbol{J}_l$. When a profile crosses the boundary of the conjugate source with a certain angle α (Figure 4), the magnetic anomaly observed on the profile ($\boldsymbol{F}$) is expressed as

$$\boldsymbol{F} = SG\delta \boldsymbol{J} \quad (16)$$

where S is the transform matrix about the strike of the boundary and G is the geometry matrix of the conjugate sources. The first spatial derivative of $\boldsymbol{F}$ has a similar form:

$$\frac{\partial \boldsymbol{F}}{\partial p} = SG_d\delta \boldsymbol{J} \quad (17)$$

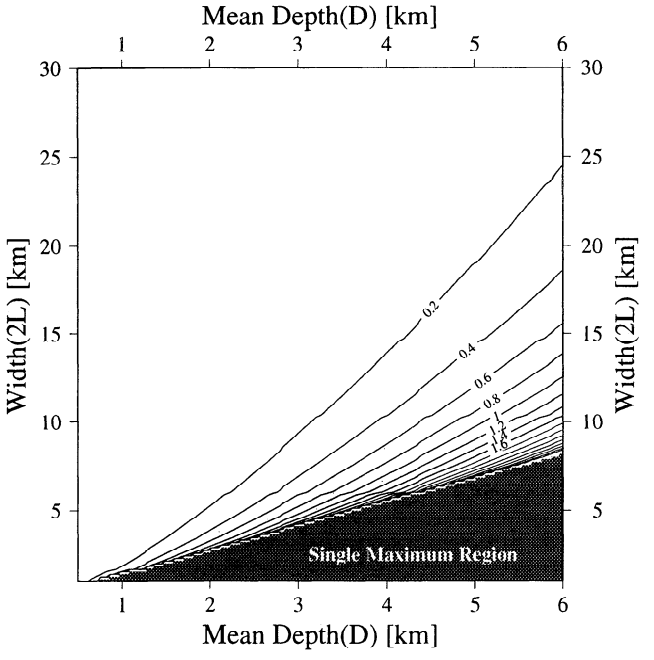

Figure 3. Result of the model calculations using the magnetic structure shown in Figure 2. Position error (Δp) is shown as contours, and contour interval is 0.2 km. ISDV profile has only single peak in shaded region.

where G_d is the geometry matrix for the spatial variation (see Appendix B for details). Equation (17) is more appropriate than (16) when the relative variation is more accurate than the absolute amplitude.

Seama et al. [1993] showed how to calculate the strike of the boundary from the data across the boundary. The relation between the observed anomaly and the strike vector of the boundary, $\boldsymbol{b}$, can be extracted from (17):

$$\left(\frac{\partial \boldsymbol{F}}{\partial p}\right) \cdot \boldsymbol{b} = 0 \tag{18}$$

which is virtually equivalent to equation (5) of *Seama et al.* [1993] (see Appendix B). The least squares inversion of the boundary strike using (18) is described in the form

$$A^T A \boldsymbol{b} = 0, \tag{19}$$

where the matrix A contains $\partial \boldsymbol{F}/\partial p$ and A^T is the transposition of A. In an ideal case, the eigenvector corresponding to the zero eigenvalue of $A^T A$ is the solution for $\boldsymbol{b}$. Since there will be errors in A due to data noise and the three dimensionality of the actual magnetic sources, $A^T A$ will not always have a zero eigenvalue, and thus we choose the eigenvector with the smallest eigenvalue as the probable solution.

In order to estimate the uncertainty in the solution, we use the theory of the Fisher distribution [*Fisher*, 1953]. The residual of the left-hand side of (18) is related to the length of resultant vector, R, by

$$R = \sum_{i=1}^{N} \sqrt{1 - \epsilon^2}, \tag{20}$$

where

$$\epsilon = \frac{\dfrac{\partial \boldsymbol{F}}{\partial p} \cdot \boldsymbol{b}}{\left|\dfrac{\partial \boldsymbol{F}}{\partial p}\right| |\boldsymbol{b}|} \tag{21}$$

and N is the number of data used in the inversion for boundary strike. The precision parameter (k), the angular standard deviation (s), and the 95 % confidence limit (α_{95}) are calculated by the following:

$$k = \frac{N-1}{N-R} \tag{22}$$

$$s \approx \frac{81^\circ}{\sqrt{k}} \tag{23}$$

$$\alpha_{95} \approx \frac{140^\circ}{\sqrt{kN}} \tag{24}$$

Estimation of Magnetization Contrasts

The ISDV profile has maxima over three important types of magnetic boundaries [*Seama et al.*, 1993] (Figure 5): (1) geomagnetic field reversals recorded by seafloor spreading, (2) topographic relief (e.g., fracture zones, abyssal hill faults), and (3) variations of the magnetization within a polarity chron (e.g., axial magnetization high, rift propagation into the same polarized seafloor). Little attention has been

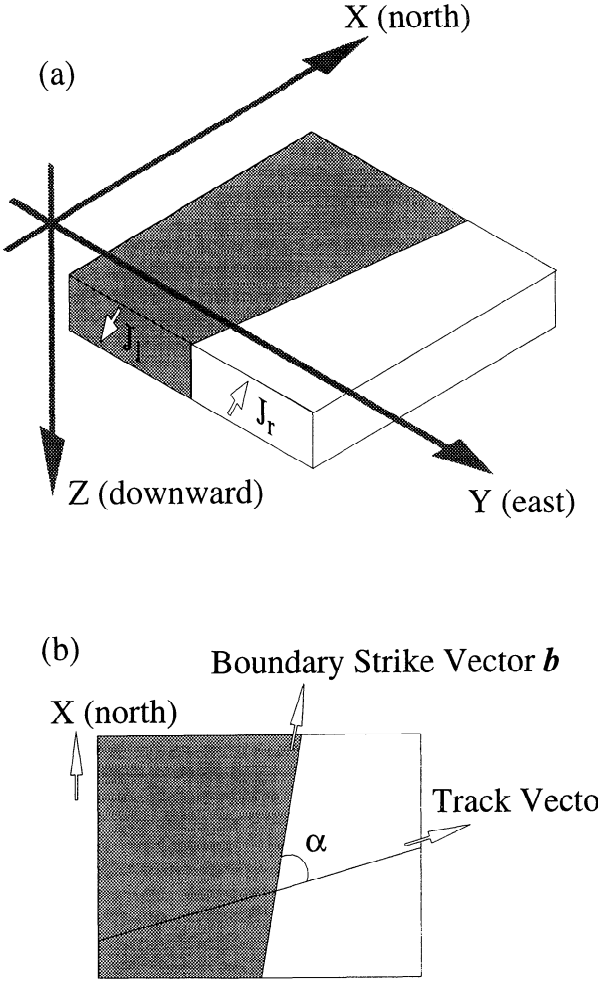

Figure 4. (a) Schematic diagram of magnetic conjugate sources. (b) Plan view of Figure 4a with ship track.

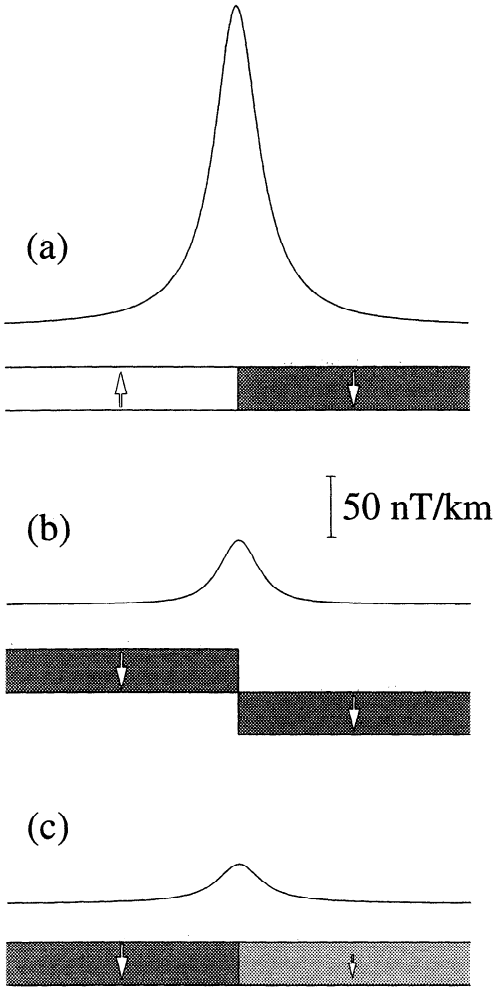

Figure 5. ISDV profiles over two-dimensional sources. Magnetic boundaries can be classified into three types. In each case, depth to the top of magnetic layer is 3 km and layer thickness is 1 km. (a) Geomagnetic field reversal origin; magnetization intensity is 8 A/m. (b) Topographic relief origin; depth to the right side is 4 km to create 1 km relief. (c) Magnetization contrast origin; magnetic intensity of the left side is 8 A/m while the right side is 6 A/m.

given to the discrimination of reversal boundaries from other kinds of magnetic sources, but to do so is absolutely necessary in the interpretation of marine magnetic anomalies. We present a method to estimate the magnetization contrasts at boundaries and classify magnetic boundaries according to the intensity of magnetization contrasts. A boundary having high contrast implies the presence of a geomagnetic field reversal, while that having low contrast may be caused by sources of the second or the third kind or may correspond to a very short reversal event.

The magnetization contrast of a boundary cannot be directly obtained from the amplitude of the ISDV. For a single magnetized layer with a constant thickness, the peak amplitude of the ISDV is controlled not only by the intensity of the contrast but also by the following three conditions: (1) the angle between the boundary and the ship track, (2) the distance to any nearby boundaries, and (3) the depth to the magnetized layer.

To estimate the intensity of the contrasts correctly, we utilize the positions and strikes of the boundaries and expand a seafloor magnetization model into a series of magnetic conjugate sources (Figure 6). Equations (16) and (17) are extended to the case of multiple boundaries,

$$\boldsymbol{F} = \sum_{i=1}^{M} S^i G^i \boldsymbol{\delta J}^i \tag{25}$$

$$\frac{\partial \boldsymbol{F}}{\partial p} = \sum_{i=1}^{M} S^i G_d^i \boldsymbol{\delta J}^i \tag{26}$$

where M is the number of the boundaries in a profile. The matrices G^i and G_d^i can be calculated on the assumption of a single magnetized layer with constant depth and thickness. The constant depth is set to the deepest depth in a survey area, and the observed anomaly $\boldsymbol{F}$ or its variation $\partial \boldsymbol{F}/\partial p$ should be upward continued using the bathymetric relief. The thickness of the layer is a rather arbitrary factor, but this method is not greatly sensitive to the value selected. In particular, the ratio of the magnetic contrasts ($|\boldsymbol{\delta J}^i|/|\boldsymbol{\delta J}^j|$) is essentially independent of the adopted thickness. Thus the magnetization contrast vectors $\boldsymbol{\delta J}^i$ can be estimated by least squares inversion using (25) or (26).

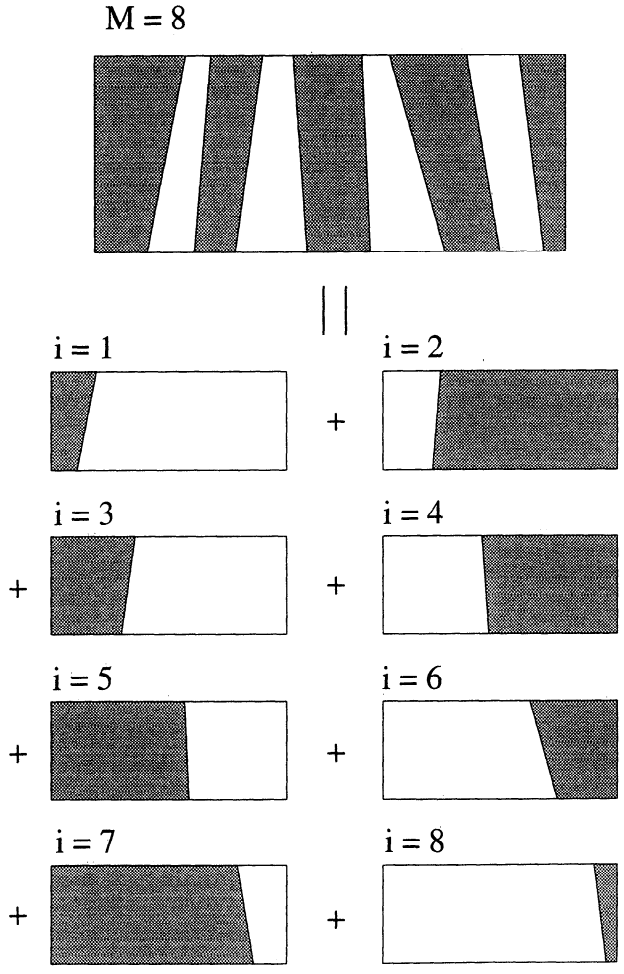

Figure 6. Schematic diagram for expansion of magnetization block model into the series of conjugate magnetic sources (showing the case of eight boundaries, i.e., M=8 in equation (25))

An Example

We applied the above procedures of data inspection and analysis to the STCM data collected during leg 5 of the GLORIA expedition aboard the R/V *Melville* (February-March 1993) that surveyed the world's fastest spreading center along the East Pacific Rise 26°-32°S [*Klaus et al.*, 1991]. Figure 7b shows a part of the ship tracks over the propagator system, and the profile labeled A was used for the following examples.

Figure 8 illustrates unfiltered magnetic vector anomalies, ship attitude data, and the comparison between two kinds of total intensity magnetic anomalies. We extracted 40 profiles from the cruise, each 170 km in length, and estimated the power spectra and the coherency between the magnetic data and the ship attitude data by averaging the results of these profiles thereby reducing the standard deviation to 15.8 % of the estimated value. The coherency between F_{PPM} and the ship attitude data (Figure 9d), which should be zero theoretically, is small but nonzero (~0.15). Thus in the following procedures, coherency less than 0.15 was set to zero. Figures 9a and 9b show two kinds of noise power, $|N_\Theta(k)|^2$ and $|N_S(k)|^2$, and the optimal filter was constructed using equation (7) (Figure 9c). N_S and F_{PPM} are strongly correlated

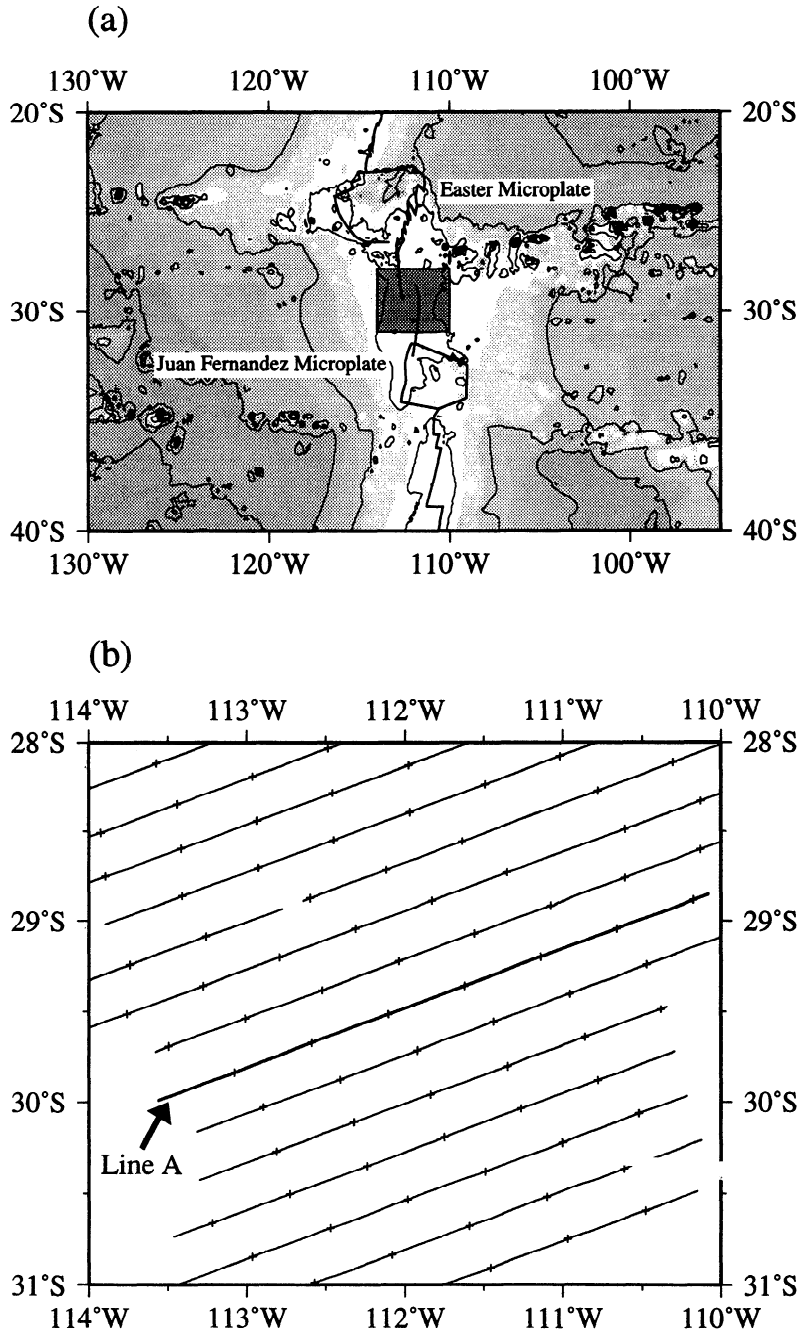

Figure 7. (a) Location of study area on southern East Pacific Rise. (b) Geomagnetic vector field data were obtained with track spacing of 28 km. Tick marks were put on tracks every 50 km. The data on the thick line (line A) were used in the examples of processing.

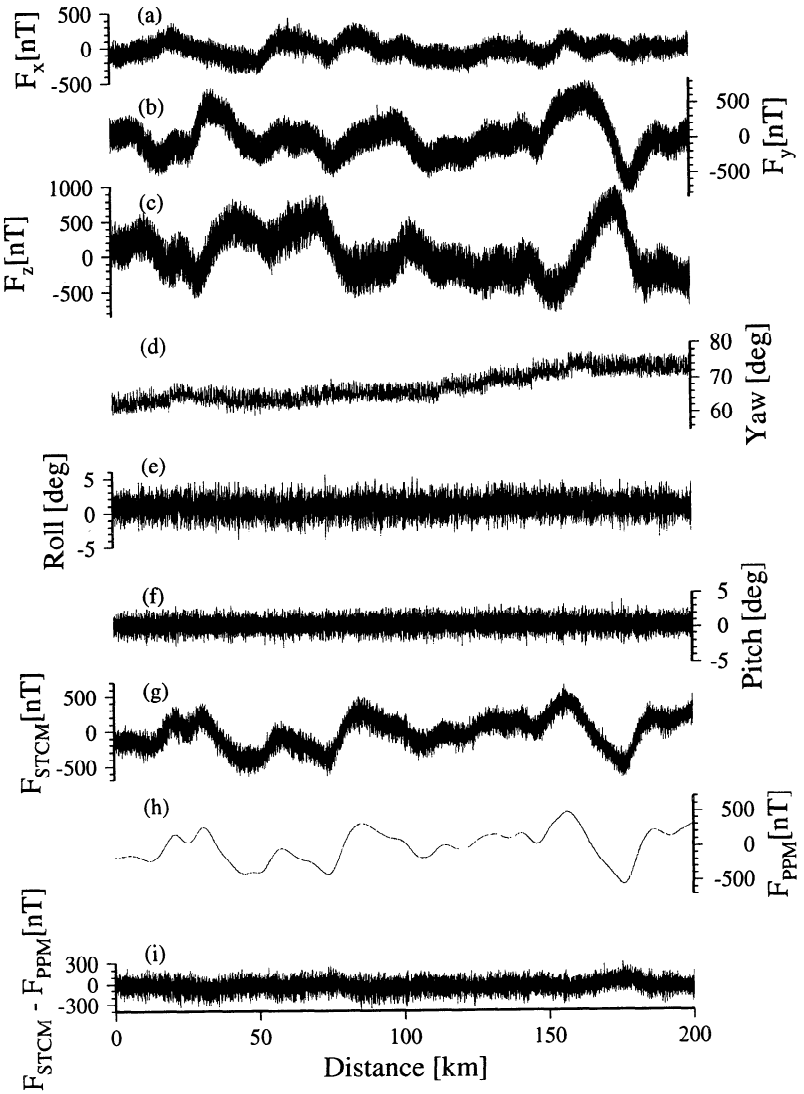

Figure 8. (a)-(c) Unfiltered magnetic vector anomalies (north, east, and downward components). (d)-(f) Ship attitude data (yaw, roll, and pitch). (g) Total intensity anomaly from the STCM. (h) Total intensity anomaly from the PPM. (i) Difference between the above two kinds of anomalies.

for wavelengths of 0.2-2 km (Figure 9e). With a ship speed of 10 knots, this wavelength range corresponds to periods of 40-400 s. This correlation can be interpreted in terms of the time dependency of the ship magnetization factors; A and $\boldsymbol{H}_p$ seem to stay constant for periods shorter than 400 s, and the resultant difference D reflects the anomaly field variation F_{PPM}. Low coherency for wavelengths less than 0.2 km results from the low sampling rate for the PPM ($\sim$0.05 Hz). Considering this correlated feature of N_S, the filter was set to zero for wavelengths less than 2 km. Furthermore, to avoid ringing in the filtered data, cosine-tapered low pass filter [*Schouten and McCamy*, 1972] was fitted to $\Phi(k)$ (Figure 9c). Because the residual noise power increases as the wavelength increases (Figure 9f), the relative variation of the data is more accurate than the absolute amplitude. ΔEa and ΔEr are 48 nT and 26 nT/km, respectively.

The 3-D index clearly shows where the 2-D assumption is valid (Figure 10e). High 3-D index may correlate with seamounts or with the sheared geometry caused by the rift propagation. Magnetic boundaries were identified from the ISDV profile with the ΔEr criterion (Figure 10g). Since most of the intervals between known reversal boundaries are wider than 10 km and the average bathymetry is about 3 km, the position error is negligible in this case (Figure 3). The full spreading rate in the area of this survey is so fast (about 160 km/m.y. [*DeMets et al.*, 1990]) that only magnetic chrons narrower than Jaramillo are blurred. The strikes of the boundaries were computed using data near the identified boundaries. The search radius for these data was set as half the distance to the adjacent boundaries, with an upper limit of 7.5 km. Figure 11a, a magnetic boundary strike map (MBSM), shows the estimated strikes with cross bars which indicate the uncertainty of the strikes; the length of a cross bar is the sine of the angular standard deviation of the inversion.

Since the relative variation is more accurate than the absolute amplitude in these data sets, equation (26) was used to estimate the magnetization contrasts at the boundaries. First, the topographic effect of the seafloor was attenuated from

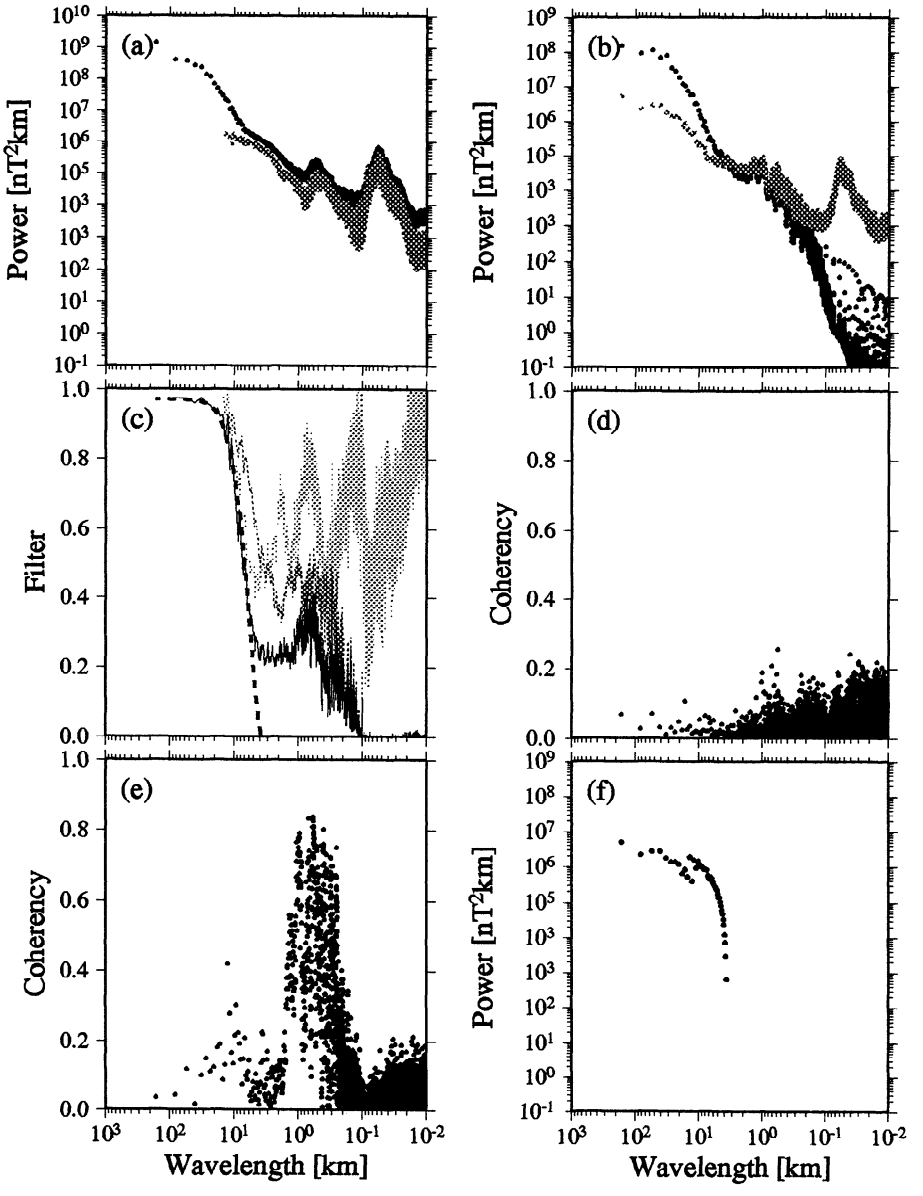

Figure 9. (a) Solid circle, power spectrum of the unfiltered magnetic vector anomalies; shaded circle, noise power spectrum estimated by the coherency with ship motion ($|N_\Theta|^2$). (b) Solid circle, power spectrum of the total intensity anomaly calculated from the PPM; shaded circle, noise power spectrum associated with scaling error ($|N_S(k)|^2$). (c) Light gray line, $\Phi_\Theta(k)$; medium gray line, $\Phi_S(k)$; solid line, optimal filter $\Phi(k)$; thick dashed line, fitted cosine-taper filter (maximum amplitude is 0.97, cut wavelength is 4 km, and pass wavelength is 50 km). (d) Squared coherency between F_{PPM} and ship motion. (e) Squared coherency between F_{PPM} and N_S. (f) Residual noise power.

the relative variation using 2-D upward continuation (Figures 11b-11d). The magnetization contrasts of the boundaries were then estimated (Figure 11e) and the MBSM was modified to include the information of these contrasts by the bar shading (Figure 11f). The superposition of the gridded 3-D index on the modified MBSM successfully showed the configuration of the seafloor magnetization in the surveyed area (Figure 12). It should be noted that the track interval is about as much as 28 km, which was appropriate for this GLORIA sidescan survey. Even with this sparse track density, the striking characters of this propagator system can be clearly seen, i.e., the high magnetization contrast of the propagator tip and the intense shear deformation of the transferred lithosphere. *Korenaga and Hey* [1993] discuss the application of these results to the tectonic history.

Discussion

We have adhered to the 2-D block model of seafloor magnetization throughout the data analysis because it is the best and perhaps only way to utilize the data of STCM. Several authors have suggested that the details of the magnetized layer are more complicated [e.g., *Johnson and Merrill*, 1978; *Schouten et al.*, 1982], but sea surface measurements are well

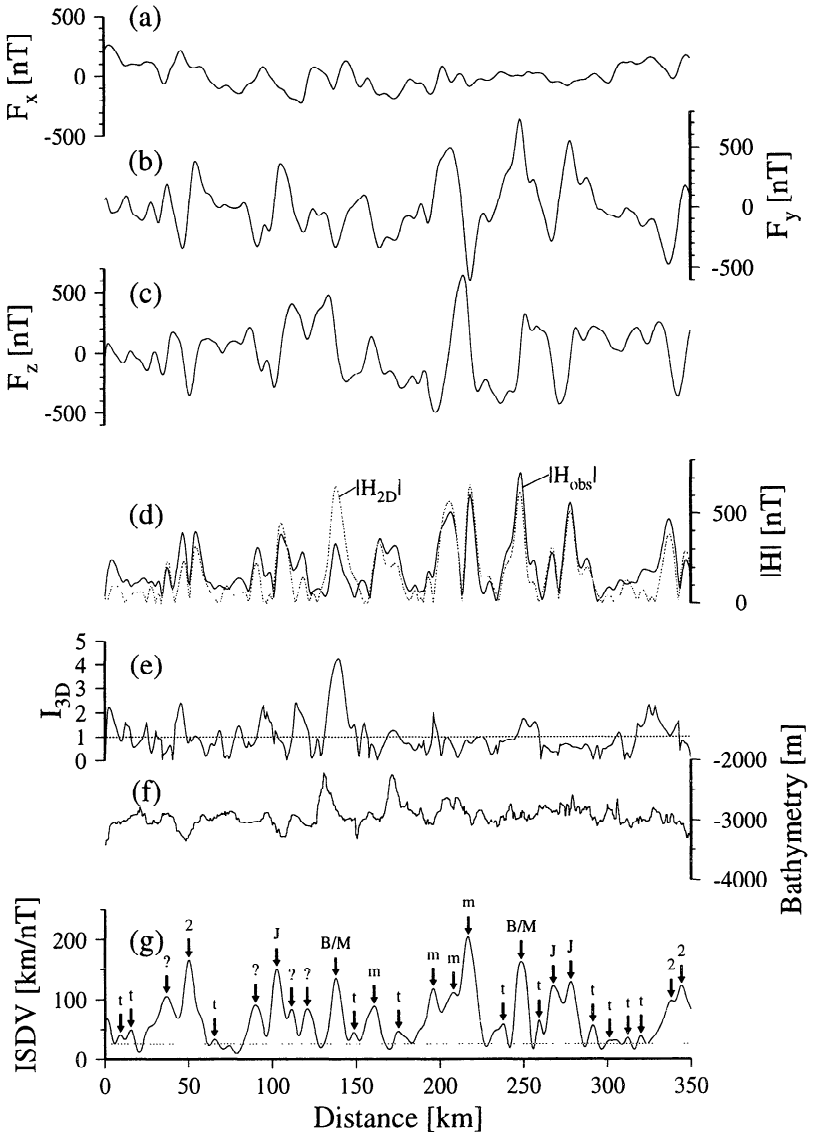

Figure 10. (a)-(c) Filtered three components of magnetic vector anomalies. (d) Observed and two-dimensional horizontal components. (e) Three-dimensional index calculated from Figure 10d by equation (12). (f) Bathymetry. (g) Magnetic boundaries were detected by ISDV profile. Critical error level (26 nT/km) is shown as dotted line. Types of boundaries are inferred from three-component profiles, estimated magnetization contrasts, and bathymetry. B/M, J(Jaramillo), and 2(anomaly 2) are geomagnetic reversal origin. Labels m and t signify magnetization contrast origin and topographic relief origin, respectively. Question marks signify boundaries with ambiguous origin.

modeled by the simplified block model. The relatively low resolution of the STCM data (Figure 9) is appropriate to view this approximate configuration of the magnetization, and the existence of the strong ISDV peaks supports this approach. We emphasize that the analysis provides an objective and automatic way of modeling; the positions and the strikes of the boundaries are used to construct a 2-D block model, and the intensity of the boundaries is estimated by least squares inversion. We also have a method to test the validity of the model by the 3-D index. "Precise" determination of the positions of magnetic boundaries with ISDV profiles [*Seama et al.*, 1993] is not always possible due to the multiple boundary problem and STCM error levels discussed previously. The detected boundaries, however, still provide a regional pattern of magnetic signatures because the calculated strikes have good reliability for 2-D magnetic fields, and our approach utilizes this aspect of STCM data.

The three dimensionality of the magnetic field can be treated with three-dimensional inversion of gridded data in the Fourier domain [*Macdonald et al.*, 1980]. Unfortunately, the current error level of STCM data caused by the time-dependent magnetization of the ship makes it difficult to construct accurate grids. The interpolation between ship tracks produces serious artifacts which prohibit downward continuation with moderate filtering.

Seama et al. [1993] proposed using the uncertainty of a boundary strike and its inclination as a discriminator for the three dimensionality of magnetic sources. However, the uncertainty is not a necessary and sufficient condition for two dimensionality of magnetic sources; the boundary strike of

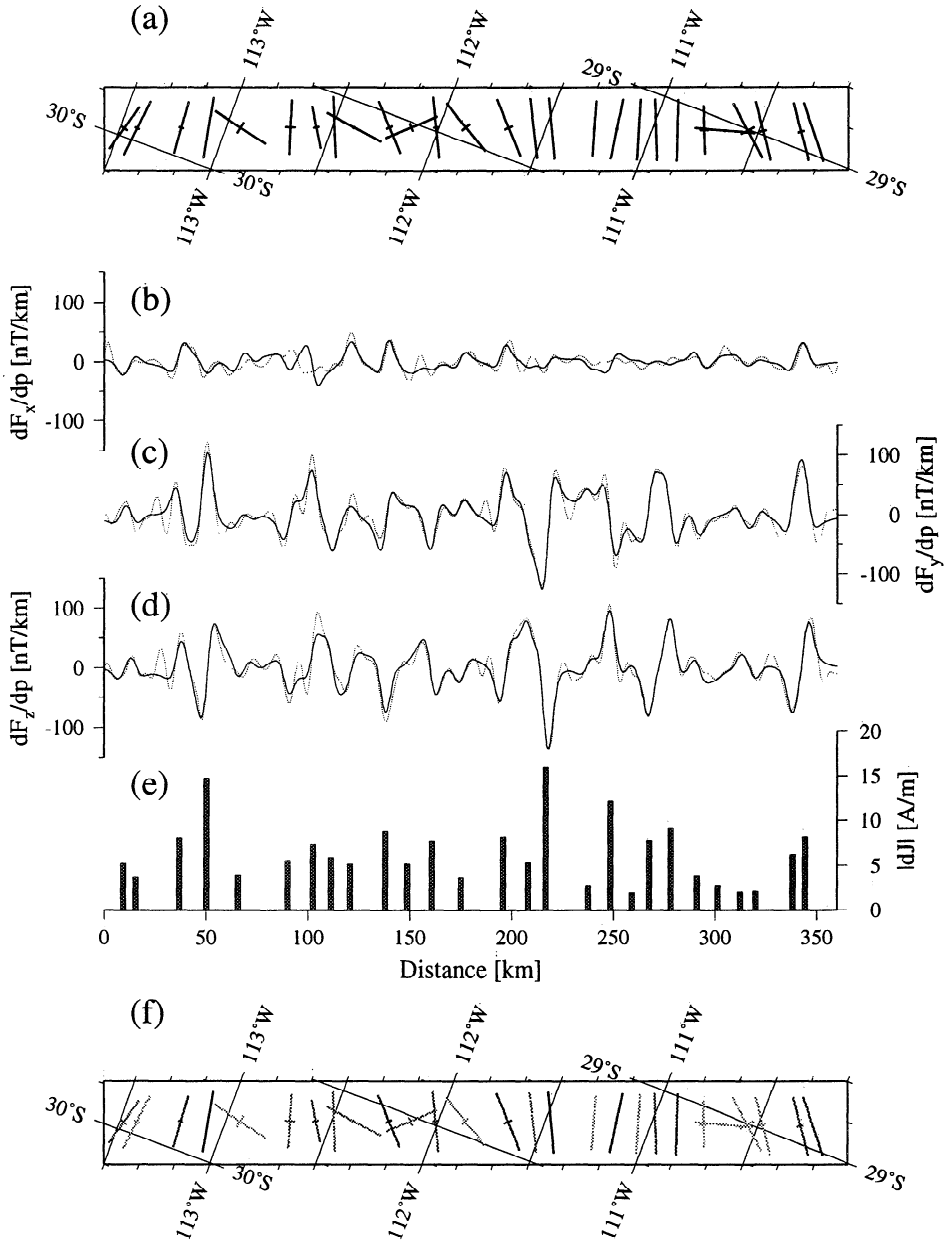

Figure 11. (a) Magnetic boundary strike map (MBSM). Bars show these strikes and length of bar corresponds to cosine of the inclination. Cross bars visualize angular standard deviation of inversion; longer cross bar signifies larger standard deviation. (b)-(d) Dotted line, upward continued relative variation of vector anomalies; solid line, fitted variation of the inversion. (e) Intensity of magnetization contrasts. (f) Modified MBSM; bar shading reflects estimated magnetization contrasts.

a 2-D magnetic source definitely has a small uncertainty, but that of a 3-D magnetic source also could have similar uncertainty. The class of 3-D magnetic sources includes all sources not purely two-dimensional, and thus a wide range of magnetic anomalies is likely. The discrimination between the dimensionality of magnetic sources cannot be done without the phase correlation of the vertical and horizontal components, such as the 3-D index method described herein.

Recent development of seafloor mapping system, such as multibeam sonar and sidescan sonar, have allowed more widely spaced tracks in marine geophysical surveys. Traditional magnetic data from these wider spaced surveys can be difficult to interpret, but vector data and the 3-D index can provide strike information along profiles regardless of track line spacing.

Conclusion

We have successfully established a comprehensive system for analyzing marine magnetic vector anomalies observed by the STCM. First, the data quality has been assessed by the estimation of the noise power spectra. The characters of the signal and noise in the wavenumber domain determine the most appropriate filter form and provide some definitive

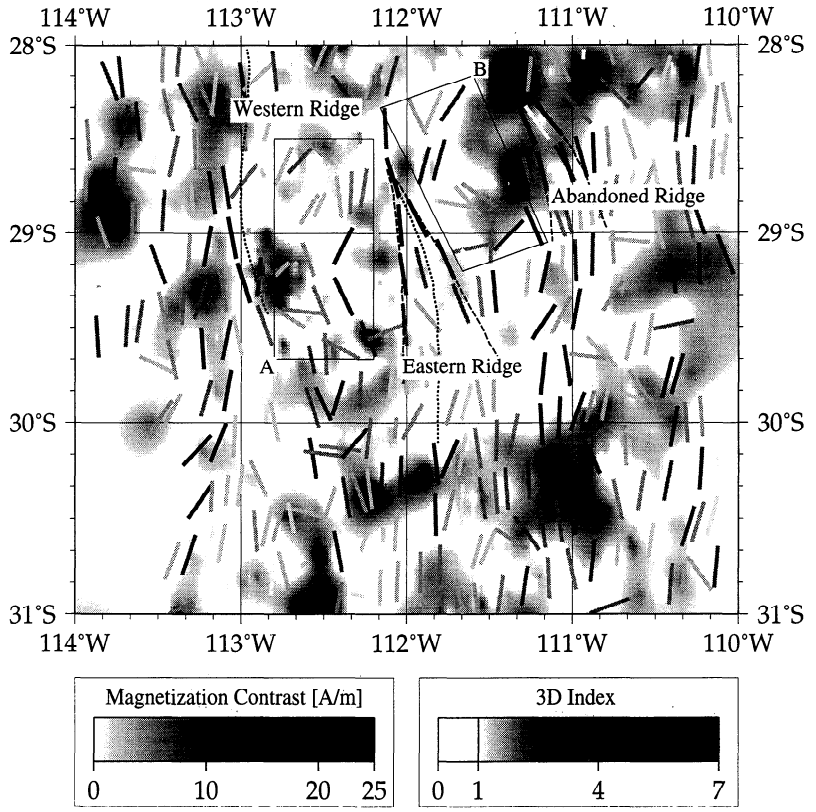

Figure 12. All the results of the four analysis methods are combined to show the configuration of the seafloor magnetization in the surveyed area. Three-dimensional index profiles were gridded to make gray-scale image of three dimensionality. Darker shade signifies higher deviation from two dimensionality. Modified MBSM was superimposed on this image. Direction of bar shows the declination of boundary strike, and its length varies with cosine of the inclination. Bar shading indicates the intensity of magnetization contrast at boundaries; darker bar signifies magnetic boundary with strong contrast. Strikes with angular standard deviation of less than 10°are shown in this map. High magnetization contrasts at eastern ridge are clearly seen around 29°S, 112°W, where are interpreted as acute-angled pseudofaults. Western ridge tip located at 29°30′S, 112°50′W has rather ambiguous contrast. Boundary strikes in the overlapping zone (box A) and to the east of Eastern ridge (box B) are significantly rotated, suggesting intense shear deformation. Abandoned ridge located at 28°30′S, 111°10′W creates magnetic field with strong three dimensionality. The area beyond this propagator system seems to have normal two dimensionality.

criteria such as the absolute error and the relative variation error.

Second, an approach for determining the magnetization of oceanic crust has been constructed, on the basis of the dominant linear character of magnetic anomalies. This approach consists of the following four steps: (1) the discrimination between 2-D/3-D magnetic sources, (2) the detection of magnetic boundaries with the ISDV profile, (3) the estimation of the boundary strike vectors, and (4) the inversion of the magnetization contrasts at the boundaries. The block model used in the fourth step is determined by the results of the second and third steps, and the validity of the model is examined by the result of the first step. All the information acquired by the above analysis is combined to a magnetization configuration map, which has great potential in decoding the tectonics of oceanic lithosphere, especially where complex tectonics is expected and where track coverage is sparse.

Appendix A: ISDV Due to Double Magnetic Boundaries

The horizontal (F_y) and vertical (F_z) components of magnetic anomaly observed at sea surface due to the two-dimensional source specified in Figure 2 are

$$F_y = PJ_y + QJ_z \quad \text{(A1)}$$

$$F_z = QJ_y - PJ_z, \quad \text{(A2)}$$

where J_y and J_z are the horizontal and vertical component of the magnetization, respectively, and

$$\begin{aligned} P = {} & \log[(y+L)^2 + (D+H/2)^2] \\ & - \log[(y+L)^2 + (D-H/2)^2] \\ & + \log[(y-L)^2 + (D-H/2)^2] \\ & - \log[(y-L)^2 + (D+H/2)^2] \end{aligned} \quad \text{(A3)}$$

$$Q = -\arctan\left[\frac{D+H/2}{y+L}\right] + \arctan\left[\frac{D-H/2}{y+L}\right] - \arctan\left[\frac{D-H/2}{y-L}\right] + \arctan\left[\frac{D+H/2}{y-L}\right]. \quad \text{(A4)}$$

The derivatives along the horizontal axis (y) are

$$\frac{\partial F_y}{\partial y} = \frac{\partial B}{\partial y}J_y + \frac{\partial A}{\partial y}J_z = |J|\left(\frac{\partial B}{\partial y}\cos I_e + \frac{\partial A}{\partial y}\sin I_e\right) \quad \text{(A5)}$$

$$\frac{\partial F_z}{\partial y} = \frac{\partial A}{\partial y}J_y - \frac{\partial B}{\partial y}J_z = |J|\left(\frac{\partial A}{\partial y}\cos I_e - \frac{\partial B}{\partial y}\sin I_e\right), \quad \text{(A6)}$$

where $|J|$ and I_e are the intensity and the effective inclination of the magnetization, respectively.
Denoting

$$R(y)\sin\beta(y) = \frac{\partial A}{\partial y} \quad \text{(A7)}$$

and

$$R(y)\cos\beta(y) = \frac{\partial B}{\partial y}, \quad \text{(A8)}$$

equations (A5) and (A6) can be expressed as

$$\frac{\partial Y}{\partial y} = |J|R(y)\sin[\beta(y) - I_e] \quad \text{(A9)}$$

$$\frac{\partial Z}{\partial y} = |J|R(y)\cos[\beta(y) - I_e] \quad \text{(A10)}$$

in which

$$R(y) = \left[\left(\frac{\partial A}{\partial y}\right)^2 + \left(\frac{\partial B}{\partial y}\right)^2\right]^{\frac{1}{2}} \quad \text{(A11)}$$

and

$$\beta(y) = \arctan\left[\left(\frac{\partial A}{\partial y}\right) / \left(\frac{\partial B}{\partial y}\right)\right]. \quad \text{(A12)}$$

Using the first-order Taylor expansion, $R(y)$ can be expressed as

$$R(y) \simeq \frac{8LH\sqrt{y^2+D^2}}{[(y+L)^2+D^2][(y-l)^2+D^2]}. \quad \text{(A13)}$$

Finally,

$$\text{ISDV} = |J|R(y) \quad \text{(A14)}$$

and the ISDV has maxima when

$$y = \begin{cases} \pm\left[\frac{L^2}{3} - D^2 + \frac{2L}{3}\sqrt{L^2+3D^2}\right]^{\frac{1}{2}} & \\ \qquad (L > (2\sqrt{3}-3)^{\frac{1}{2}}D) & \\ 0 \qquad (L \le (2\sqrt{3}-3)^{\frac{1}{2}}D) & \end{cases} \quad \text{(A15)}$$

Appendix B: Magnetic Anomaly Due to Conjugate Magnetic Sources

The explicit forms of S, G, G_d in equations (16) and (17) are

$$S = \begin{pmatrix} \frac{b_x}{\sqrt{b_x^2+b_y^2}} & \frac{-b_y}{\sqrt{b_x^2+b_y^2}} & 0 \\ \frac{b_y}{\sqrt{b_x^2+b_y^2}} & \frac{b_x}{\sqrt{b_x^2+b_y^2}} & 0 \\ 0 & 0 & 1 \end{pmatrix} \cdot \begin{pmatrix} \sqrt{b_x^2+b_y^2} & 0 & -b_z \\ 0 & 1 & 0 \\ b_z & 0 & \sqrt{b_x^2+b_y^2} \end{pmatrix} = \begin{pmatrix} b_x & \frac{-b_y}{\sqrt{b_x^2+b_y^2}} & \frac{-b_x b_z}{\sqrt{b_x^2+b_y^2}} \\ b_y & \frac{b_x}{\sqrt{b_x^2+b_y^2}} & \frac{-b_y b_z}{\sqrt{b_x^2+b_y^2}} \\ b_z & 0 & \sqrt{b_x^2+b_y^2} \end{pmatrix} \quad \text{(B1)}$$

$$G = \begin{pmatrix} 0 & 0 & 0 \\ 0 & -A & B \\ 0 & B & A \end{pmatrix} \quad \text{(B2)}$$

$$G_d = \begin{pmatrix} 0 & 0 & 0 \\ 0 & -A' & B' \\ 0 & B' & A' \end{pmatrix} \quad \text{(B3)}$$

where (b_x, b_y, b_z) is the boundary strike vector in Figure 4b, A, B, A', B' are functions of the horizontal distance in a normal direction between the boundary and the observation point (p), the depth to the upper surface (h_1), and the lower surface (h_2) of the magnetized layer [e.g., *Vacquier*, 1972],

$$A = 2\left[\arctan\left(\frac{p}{h_1}\right) - \arctan\left(\frac{p}{h_2}\right)\right] \quad \text{(B4)}$$

$$B = \ln\frac{p^2+h_2^2}{p^2+h_1^2} \quad \text{(B5)}$$

$$A' = 2\left(\frac{h_1}{p^2+h_1^2} - \frac{h_2}{p^2+h_2^2}\right)\sin\alpha \quad \text{(B6)}$$

$$B' = 2\left(\frac{p}{p^2+h_2^2} - \frac{p}{p^2+h_1^2}\right)\sin\alpha \quad \text{(B7)}$$

(B8)

and where α is the intersecting angle of the boundary strike vector and the ship track vector shown in Figure 4.

Equation (17) can be written as

$$S^{-1}\left(\frac{\partial \boldsymbol{F}}{\partial p}\right) = G_d \boldsymbol{dJ}. \quad \text{(B9)}$$

Equation (18) is the first equation of the above linear system. It can be also derived from equation (5) of *Seama et al.* [1993] by spatial differentiation along a profile:

$$\frac{\partial}{\partial p}(\boldsymbol{F}\cdot\boldsymbol{b} + (\text{const})) = \left(\frac{\partial \boldsymbol{F}}{\partial p}\right)\cdot\boldsymbol{b} = 0. \quad \text{(B10)}$$

Acknowledgments. Nobuhiro Isezaki generously provided us with his STCM. Keizo Sayanagi supported the installation of the STCM on the R/V *Melville* in many aspects. Kensaku Tamaki and Hiromi Fujimoto kindly coordinated our participation to the 1993 R/V *Melville* GLORIA expedition, through the contract 04044044 (InterRidge Japan Project) of the Ministry of Education, Science and Culture. This participation was also partially supported by NSF grants to David Naar, OCE-9116012 and OCE-9302802. Leg 5 of the GLORIA expedition was funded by NSF grant OCE-9101341 to Richard Hey. The captain and crew of the R/V *Melville* and the SIO shipboard technician group assisted the installation and operation of the STCM. Kensaku Tamaki, Nobuhiro Isezaki, Philip Jarvis, David Naar, Richard Hey, and Dan Scheirer reviewed the manuscript and provided useful comments. Patrick Taylor, Richard Blakely, and John Mariano are thanked for their thorough reviews and critical comments.

References

Atchuta Rao, D., H. W. Ram Babu, and P. V. Sanker Narayan, Interpretation of magnetic anomalies due to dikes: The complex gradient method, *Geophysics*, *46*, 1572–1578, 1981.

Blakely, R. J., A. Cox, and E. J. Iufer, Vector magnetic data for detecting short polarity intervals in marine magnetic profiles, *J. Geophys. Res.*, *78*, 6977–6983, 1973.

DeMets, C., R. G. Gordon, D. F. Argus, and S. Stein, Current plate motions, *Geophys. J. Int.*, *101*, 425–478, 1990.

Fisher, R. A., Dispersion on a sphere, *Proc. R. Soc. London A*, *217*, 295–305, 1953.

Hey, R. N., F. K. Duennebier, and W. J. Morgan, Propagating rifts on midocean ridges, *J. Geophys. Res.*, *85*, 3647–3658, 1980.

International Association of Geomagnetism and Aeronomy Division V, International geomagnetic reference field, 1991 revision, *J. Geomagn. Geoelectr.*, *43*, 1007–1012, 1991.

Isezaki, N., A new shipboard three-component magnetometer, *Geophysics*, *51*, 1992–1998, 1986.

Johnson, H. P., and R. T. Merrill, A direct test of the Vine-Matthews hypothesis, *Earth Planet. Sci. Lett.*, *40*, 263–269, 1978.

Klaus, A., W. Icay, and R. N. Hey, SeaMARC II survey of a propagating limb of a large nontransform offset near 29°S along the fastest spreading East Pacific Rise segment, *J. Geophys. Res.*, *96*, 9985–9998, 1991.

Korenaga, J., and R. N. Hey, Analysis of geomagnetic vector anomalies at the dueling propagator system EPR 29°S (abstract.), *Eos Trans. AGU*, *74(43)*, *Fall Meeting suppl.*, 672, 1993.

Lonsdale, P., Overlapping rift zones at the 5.5°S offset of the East Pacific Rise, *J. Geophys. Res.*, *88*, 9393–9406, 1983.

Macdonald, K. C., and P. J. Fox, Overlapping spreading centers: New accretion geometry on the East Pacific Rise, *Nature*, *301*, 55–58, 1983.

Macdonald, K. C., S. P. Miller, S. P. Huestis, and F. N. Spiess, Three-dimensional modeling of a magnetic reversal boundary from inversion of deep-tow measurements, *J. Geophys. Res.*, *85*, 3670–3680, 1980.

Nabighan, M. N., The analytic signal of two-dimensional magnetic bodies with polygonal cross-section: Its properties and use for automated anomaly interpretation, *Geophysics*, *37*, 507–517, 1972.

Press, W. H., S. A. Teukolsky, W. T. Vetterling, and B. P. Flannery, *Numerical Recipes in C, 2nd ed.*, Cambridge University Press, New York, 1992.

Schouten, H., and K. McCamy, Filtering marine magnetic anomalies, *J. Geophys. Res.*, *77*, 7089–7099, 1972.

Schouten, H., C. Denham, and W. Smith, On the quality of marine magnetic anomaly sources and sea floor topography, *Geophys. J. R. Astron. Soc.*, *70*, 245–260, 1982.

Seama, N., and N. Isezaki, Sea-floor magnetization in the eastern part of the Japan basin and its tectonic implications, *Tectonophysics*, *181*, 285–297, 1990.

Seama, N., Y. Nogi, and N. Isezaki, A new method for preciese determination of the position and strike of magnetic boundaries using vector data of the geomagnetic anomaly field, *Geophys. J. Int.*, *113*, 155–164, 1993.

Spector, A., and F. S. Grant, Statistical models for interpreting aeromagnetic data, *Geophysics*, *35*, 293–302, 1970.

Vacquier, V., *Geomagnetism in Marine Geology*. Elsevier, New York, 1972.

Vine, F. J., and D. H. Matthews, Magnetic anomalies over oceanic ridges, *Nature*, *199*, 947–949, 1963.

J. Korenaga, Woods Hole Oceanographic Institution, Woods Hole, MA 02543

(Received February 8, 1994; revised September 21, 1994; accepted September 29, 1994.)